Energy Storage Materials 80 (2025) 104411

Contents lists available at ScienceDirect

Energy Storage Materials

journal homepage: www.elsevier.com/locate/ensm

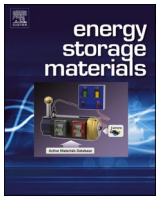

Synergistic regulation of de-solvation effect and planar deposition via in-situ interface engineering for ultra-stable dendrite-free Zn-ion batteries

Tao Yang [a,1], Tianyu Shen [a,1], Yuhang Liang [b,1], Miaojie Fang [a], Hongbo Wu [a], Ouwei Sheng [a], Hongli Chen [d], Chang Dong [a], Haojie Ji [a], Jian Zhang [a], Rongkun Zheng [c,*], Hao Liu [d,*], Guoxiu Wang [d,*], Xuefeng Zhang [a]

[a] International Research Center for EM Metamaterials & Institute of Advanced Magnetic Materials, College of Materials and Environmental Engineering, Hangzhou Dianzi University, Hangzhou 310012, China
[b] College of Chemistry, Fuzhou University, Fuzhou, Fujian, 350108, China
[c] School of Physics, The University of Sydney, Camperdown, New South Wales 2006, Australia
[d] Centre for Clean Energy Technology, University of Technology Sydney, Broadway, Sydney, NSW, 2007, Australia

ARTICLE INFO

Keywords:
Zn anode
Zn metal batteries
Coordination polymers
Interfacial layer
Zinc dendrites

ABSTRACT

Advanced interfacial engineering is essential to address key challenges such as dendrite formation, parasitic reactions, and sluggish electrochemical kinetics, in aqueous zinc-ion batteries. In this study, by using a facile self-assembly method, we developed an armor-like interfacial layer (ZSL) on the Zn surface, serving as both an ion re-distributor and a protective barrier. This compact interfacial layer exhibits suitable hydrophilic and zincophilic features, enabling consistent and uniform Zn^{2+} flux and reducing voltage polarization. The ZSL also enhances the de-solvation process, speeds up zinc deposition kinetics, and suppresses parasitic reactions induced by water decomposition. Furthermore, it decreases the surface energy, promoting planar deposition of Zn^{2+}. As a result, the modified zinc anodes demonstrate exceptional cycling stability, maintaining a dendrite-free surface for >8000 h with minimal byproduct formation. The asymmetric cell utilizing ZSL@Zn anodes exhibits highly stable reversibility over 6000 cycles with an average Coulombic efficiency (CE) of 99.89 %. In full cells paired with $Na_2V_6O_{16}{\cdot}3H_2O$ (NVO) cathodes, the Zn-ion batteries exhibit excellent rate performance and long-term cycling durability. This work highlights the significant role of in-situ interfacial layers in achieving highly stable and reversible zinc anodes for large-scale zinc-ion battery applications.

1. Introduction

Lithium-ion batteries are esteemed for their light-weight nature and high energy density, rendering them dominant electrochemical energy storage devices for portable electronics, electric vehicles and renewable energy storage [1,2]. However, their extensive commercialization for large-scale energy storage is hampered by high costs and safety concerns, including the risk of explosions [3–6]. In contrast, aqueous zinc-ion batteries (AZIBs) present a safer and more cost-effective alternative with sufficient energy density and an environmentally friendly operating environment [3,7,8]. These merits stem from the excellent theoretical capacity (820 mAh g^{-1} and 5855 Ah cm^{-3}), suitable redox potential (−0.762 V vs. standard hydrogen electrode), the abundance and strong chemical stability of metallic Zn, as well as the nonflammability of aqueous electrolytes [9–11]. Despite these virtues, commercial zinc anodes face challenges with poor reversibility during electrochemical cycling, hindering the practical adoption of AZIBs. Zinc anodes in the aqueous electrolyte are prone to side reactions, such as hydrogen evolution reaction (HER), electrochemical corrosion, and surface passivation [12]. These reactions increase internal cell pressure, reduce the usage of active zinc, and lower Coulombic efficiency (CE). In addition, the unregulated dendrite growth caused by inhomogeneous deposition at the electrode/electrolyte interface, particularly under elevated current densities, can puncture the separator and result in cell failure [13–15].

To address these challenges, various effective solutions have been proposed, including surface modification of zinc anodes[16–19], deployment of three-dimensional current collectors[20,21], innovation

* Coresponding authors.
E-mail addresses: rongkun.zheng@sydney.edu.cn (R. Zheng), hao.liu@uts.edu.au (H. Liu), guoxiu.wang@uts.edu.cn (G. Wang).
[1] These authors contributed equally to this work.

https://doi.org/10.1016/j.ensm.2025.104411
Received 24 April 2025; Received in revised form 5 June 2025; Accepted 21 June 2025
Available online 24 June 2025
2405-8297/© 2025 The Author(s). Published by Elsevier B.V. This is an open access article under the CC BY license (http://creativecommons.org/licenses/by/4.0/).

in separator materials[22,23], and incorporation of electrolyte additives [24–26], etc. Among these strategies, the construction of artificial protective layers on the zinc anode surface emerges as an easy-to-operate and highly feasible solution for large-scale manufacturing. As dendrite growth and severe side reactions are interlinked[27], these interfacial layers are designed to reduce parasitic reactions and promote uniform zinc deposition by uniformizing Zn^{2+} flux and stabilizing the local electric field.

Artificial protective layers are commonly constructed by ex-situ methods like doctor blading or spin coating, but these methods often result in poor adhesion and uneven Zn^{2+} distribution. The volumetric changes during zinc plating and stripping can cause these coatings to detach, diminishing their protective effectiveness. In contrast, constructing stable zincophilic artificial protective layers directly on the zinc surface through in-situ methods is desirable for achieving highly reversible zinc anodes [28]. Although the alloy-based interfacial layers prepared by replacement reactions[29,30] reduce the nucleation barrier and maintain a uniform interfacial electric field, however, their high conductivity promotes the preferential deposition of Zn^{2+} ions on the interfacial layers and reduces the utilization of Zn[31]. Differently, non-conductive layers not only block water penetration, but also provide abundant active sites[32,33] or pore structures[34,35] for uniform Zn^{2+} deposition, ultimately realizing a long-lasting and reversible Zn anode.

Herein, an armor-like zinc succinate coordination polymer was developed as a multifunctional protective coating, enriched with zincophilic sites, on the zinc anode surfaces through a facile self-assembly and electrochemical conversion process. The zinc succinate polymer offers several key advantages including dense structure and intrinsic carboxyl groups facilitate uniform ionic field distribution at the interface and enhance the de-solvation of hydrated Zn^{2+} ions, thereby accelerating deposition kinetics for dendrite-free Zn deposition. It also serves as a filter for capturing reactive water molecules, stabilizing the interfacial pH value and reducing parasitic reactions. Furthermore, the zinc succinate polymer reduces the surface energy of Zn and promotes the preferential growth of Zn (002) planes, significantly minimizing the occurrence of Zn dendrites and enhancing corrosion resistance. The protective layer demonstrated outstanding long-term stability, maintaining low overpotentials for over 8000 h in symmetrical cells at 1 mA cm^{-2} and a high Coulombic efficiency of 99.89 % over 6000 cycles. In the full cell with $Na_2V_6O_{16}{\cdot}3H_2O$ (NVO) cathodes, the system exhibited excellent rate capability and cycling stability, retaining 94.45 % capacity after 130 cycles, even with a low N/P ratio of 1.10 and an E/C ratio of 6.8 μL mAh^{-1}.

2. Results and discussion

2.1. Synthesis and characterizations of ZSL

The armor-like interfacial layer is formed on the zinc metal surface through an in-situ self-assembly reaction involving Zn and succinic acid, where the latter exhibits the lowest energy level of the lowest unoccupied molecular orbital (LUMO) and the smallest orbital energy gap compared to other groups, including sulfonic and phosphonic acids (Figure S1). Scanning electron microscopy (SEM) images display that the surface of zinc foil is homogenously covered by a dense armor-like interfacial layer after the reaction in a succinic acid-methanol (SA-MeOH) solution at a concentration of 5 g L^{-1} for 1 h (Figs. 1a and S2). The

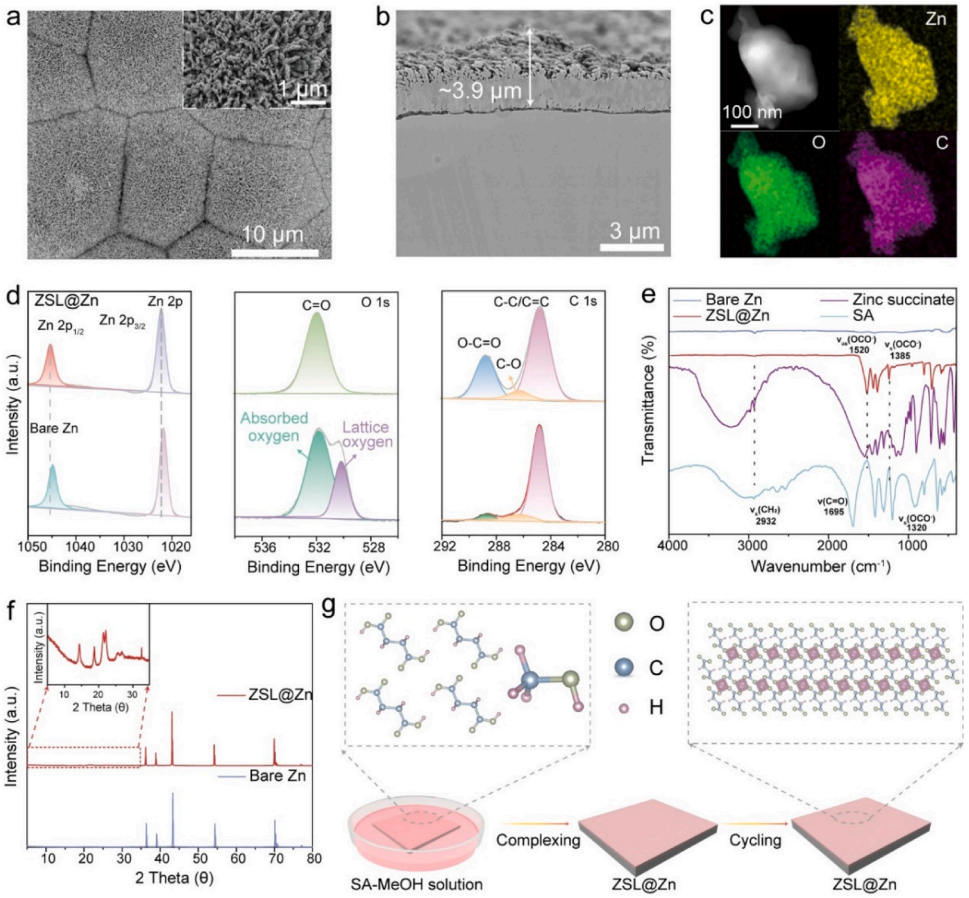

Fig. 1. (a) Top-view and (b) cross-view SEM images of the ZSL@Zn anode. (c) STEM and EDS images of ZSL nanoparticles and the corresponding mapping images of C, O, and Zn elements. (d) High-resolution XPS spectra of Zn 2p, O 1 s and C 1 s for different anodes. (e) FTIR spectra of bare Zn, succinic acid (SA), homemade zinc succinate (ZS) powder, and ZSL@Zn. (f) XRD pattern of the ZSL@Zn anode. (g) Fabrication schematic of the ZSL@Zn anode.

inset in Fig. 1a depicts that this interfacial layer is enriched with abundant hierarchical substructures. The side-view SEM and energy-dispersive X-ray spectroscopy (EDS) images show that the micron-scale interfacial layer is tightly bonded to the zinc foil with a uniform phase distribution (Figs. 1b and S3).

Benefiting from the hierarchical porous structure, the ZSL@Zn electrode exhibits a lower contact angle than that of bare Zn (Figures S4), indicating that the hydrophilic ZSL effectively improves the wettability. In general, enhanced wettability implies the reduction of the interfacial energy between the solid interfacial layer and the electrolyte, which facilitates the rapid ion transfer[36]. The homogeneous distribution of Zn, O, and C elements in ZSL is validated by scanning transmission electron microscopy (STEM) and EDS images (Fig. 1c). Appropriate preparation conditions and parameters are essential in the construction of the armor-like interfacial layers. The area of zinc foil covered by the interfacial layer increases with the reaction time, as illustrated in Figure S5. After dissolving succinic acid in different solvents and then reacting with the zinc foil for 1 h, a looser armor-like interfacial layer is obtained on the zinc surface in the ethanol (EtOH) solution, and only a small number of flower-like structures scattered sporadically on the zinc foil are found in isopropanol (IPA). In contrast, no interfacial layer is found in N, N-dimethylformamide (DMF) solutions, only many holes are found (Figure S6). This indicates that the solvent has an important effect on the formation of the interfacial layer. The effect of different concentrations of SA on the morphology and composition of the interfacial layer was subsequently investigated. The effect of concentration on the overall morphology of the interfacial layer was not significant, accompanied by increased substructure and thickness (Figure S7). For example, the thickness of the prepared interfacial layer reaches about 7.4 μm at a concentration of 40 g L^{-1} (Figure S8). When the concentration is as high as 100 g L^{-1}, an inhomogeneous morphology appears in the morphology. Besides this, attempts were also made to soak the zinc foils under different dicarboxylic acid-MeOH solutions with different carbon chains, and the SEM images of the as-obtained samples are depicted in Figure S9.

The surface of the zinc foil immersed in oxalic acid develops a loose interfacial layer with a hydrangea-like structure, whereas only massive holes are spotted on the surface of the zinc foil immersed in propanedioic acid. Besides, other zinc foil surfaces that have been soaked in dicarboxylic acid also form interfacial layers. The only difference is that the hierarchical substructure of interfacial layers gradually collapses as the carbon chain continues to increase, leaving behind a randomly stacked lamellar structure. Subsequently, the structure information of ZSL@Zn was identified by high-resolution X-ray photoelectron spectroscopy (XPS), Fourier transform infrared spectroscopy (FT-IR), and X-ray diffraction (XRD) analysis. The full XPS spectra reveal that no special impurities appeared on the surface of the immersed zinc foil (Figure S10). Compared with the high-resolution Zn 2p spectra of bare Zn, the binding energy position of ZSL@Zn presents a shift, which stems from the formation of Zn-O polar bonds in the interfacial layer that alters the coordination environment. The high-resolution O 1 s and C 1 s spectra, on the other hand, similarly prove the existence of the interfacial layer, where the signal located at 531.9 eV in the O 1 s spectrum and the strong peak centered at 288.8 eV in the C 1 s spectrum indicate the emergence of $C = O$ polar bonds on the surface of the Zn foil (Fig. 1d).

The FT-IR spectra of bare Zn, typical succinic acid (SA), the homemade zinc succinate powder (prepared by a coprecipitation method), and ZSL@Zn are presented in Fig. 1e. Apparently, a prominent peak at 2932 cm^{-1} corresponding to the symmetric stretching vibration of the CH_2 groups was detected in all the last three samples. The carbonyl ($C = O$) stretching vibration appears at 1695 cm^{-1}. Additionally, the symmetric stretching vibration of the carboxylate (OCO^-) group is observed at 1320 cm^{-1}. The FT-IR spectrum of ZSL@Zn, differing from that of zinc succinate powder, exhibits significant peaks at 1520 cm^{-1} and 1385 cm^{-1}, which are attributed to the asymmetric and symmetric stretching vibrations of the carboxylate (OCO^-) groups, respectively. The FT-IR spectra of zinc foils treated with different dicarboxylic acids showed similar characteristic peaks (Figure S11). These characteristic peaks confirm the coordination of the succinate anion with zinc ions, indicating the possible formation of zinc succinate complexes on the surface of zinc flakes following the in-situ reaction. This is verified by the XRD result and thermogravimetric curve (Figs. 1f and S12). The weak diffraction peaks of the armored interfacial layer did not coincide with those of the homemade zinc succinate powder and its standard reference card (PDF #51–2305) (Figure S13). Of note, although it is difficult to accurately determine the complex's crystalline structure, it undergoes a crystalline phase transition after cycling. As illustrated in Figure S14, the XRD results reveal that the crystalline phase of the complex is completely transformed to zinc succinate after the initial cycle and remains unchanged after several subsequent cycles. This result is also validated by the FT-IR spectra of ZSL@Zn following various cycles, where the characterization peaks coincide with those of the homemade zinc succinate powder (Figure S15). Encouragingly, the morphology of the ZSL remains intact with the phase transition (Figure S16). The schematic diagram of the formation of the final ZSL is therefore presented in Fig. 1 g, in which the succinic acid is completely deprotonated upon dissolution and the formed succinic acid anion has a strong electron-donating ability to undergo a strong coordination ability with Zn^{2+}, followed by the formation of an armor-like complex with hierarchical substructures in situ on the zinc surface by self-assembly. This complex is not stable and exhibits complete conversion upon cycling to the zinc succinate coordination polymer, whose structure comprises an indefinitely interconnected 3D framework of tetrahedrally coordinated zinc centers, with four distinct succinate ligands donating an oxygen atom to four individual Zn atoms in a bi-ligand configuration.

2.2. Interfacial chemistry and Zn deposition mechanism

Zinc anodes routinely encounter spontaneous chemical corrosion problems upon immersion in mildly acidic electrolytes. This issue disrupts the uniform electric field and accelerates zinc dendrite growth at the zinc deposition interface. The comprehensive evaluation delves into the protective effects of the armor-like interfacial layer on zinc anodes. As shown in Fig. 2a, ZSL@Zn maintains its pristine surface morphology without detectable by-products after 7 days of immersion in 2 M $ZnSO_4$ electrolyte. In contrast, numerous flaky byproducts form on the surface of bare Zn, resulting in a dark color of the zinc anode (Figure S17). The X-ray diffraction (XRD) result identifies these flaky byproducts as $Zn_4SO_4(OH)_6{\cdot}5H_2O$ (ZHS, PDF#78–0246), indicating that bare zinc is undergoing the electrochemical corrosion reaction and considerable passivation in the electrolyte (Fig. 2b). Tafel curves in Fig. 2c reveal that ZSL@Zn has a lower corrosion current density and a higher corrosion potential compared to bare Zn, indicating its superior corrosion resistance. Besides, the reduced current density in linear sweep voltammetry (LSV) curves and the larger Tafel slope demonstrate the suppressed rate of hydrogen evolution reaction (HER) for ZSL@Zn (Figs. 2d and S18). The adsorption energies of water molecules with bare Zn and ZSL@Zn were subsequently calculated by density functional theory (DFT). As illustrated in Fig. 2e, the adsorption energy of H_2O on zinc succinate (−0.47 eV) is appreciably higher than that of Zn (−0.30 eV), implying that water molecules are more likely to adsorb with zinc succinate, which effectively captures H_2O from initiating parasitic reactions.

The pH fluctuation at the electrolyte/electrode interface significantly influences the performance of the zinc anode [37]. Elevated pH values stimulate the formation of ZHS, whereas reduced pH levels exacerbate HER. Consequently, maintaining a stable pH at the electrolyte/electrode interface is imperative. In-situ pH monitoring experiments documented the variations in interfacial pH during cycling. During the initial plating process, the bare Zn electrode exhibits a sustained increase in pH attributable to HER, followed by a minor decrease before rising again during the stripping process, with a steady increase continuing into the second plating process (Fig. S19a). The interfacial

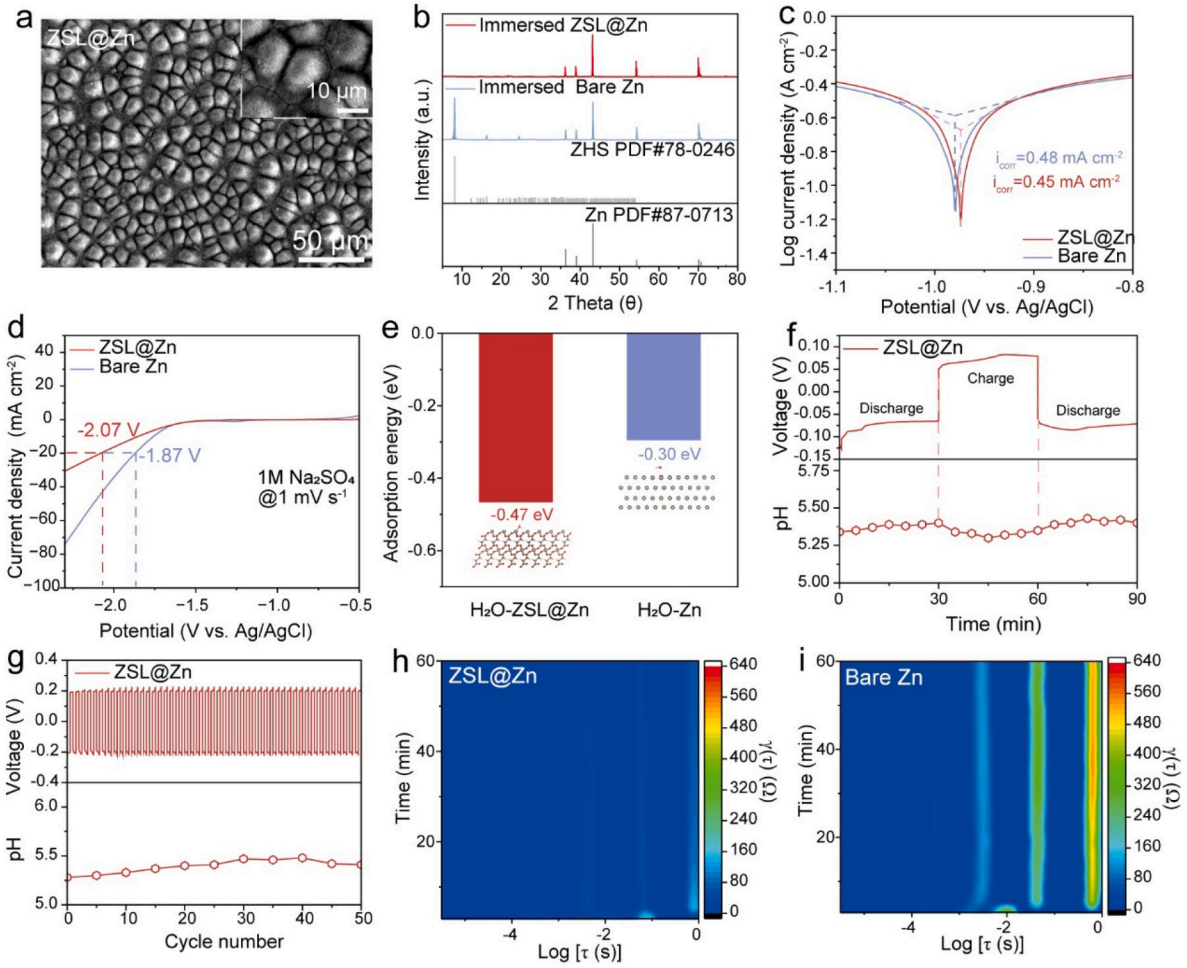

Fig. 2. (a) SEM image and (b) XRD patterns of ZSL@Zn anodes soaked in $ZnSO_4$ solution for 7 days. (c) Tafel plots and (d) LSV curves of ZSL@Zn and bare Zn anodes. (e) Adsorption energy of H_2O on the surface of ZSL@Zn and bare Zn anodes. (f) Real-time interface pH change near ZSL@Zn cycling at 2 mA cm^{-2} and 1 mAh cm^{-2}. (g) In situ pH evolution of ZSL@Zn symmetric cells cycling at 4 mA cm^{-2} and 1 mAh cm^{-2}. DRT analysis of the EIS results during the plating process of (h) ZSL@Zn and (i) bare Zn anodes.

pH variations after various cycles reveal that the pH value of the bare Zn electrode progressively escalates to 5.91 after 50 cycles (Figure S19b). In stark contrast, the ZSL@Zn electrode displays smaller pH variation at the interface under the same conditions (Figs. 2f and 2 g), demonstrating a strong interfacial pH stabilization capability.

The distribution of relaxation times (DRT) obtained by in situ electrochemical impedance spectroscopy (EIS) were utilized to probe the changes in interfacial kinetics at different time constants. The peaks with relaxation time (τ) in the range of 10^{-4} to 10^{-1} s, 10^{0}–10^{2} s belong to the charge transfer and diffusion process, respectively [38]. In the ZSL@Zn symmetric cell, the charge transfer resistance (Rct) is consistently smaller during the plating and stripping processes and continues to decrease during the corresponding stages (Figs. 2h, S20a, S21a and S21b). In contrast, the R_{ct} of bare Zn gradually increases both for plating and stripping processes (Figs. 2i, S20b, S21c and S21d). It indicates that the introduction of ZSL significantly reduces the appearance of by-products and ensures fast interfacial kinetics.

The deposition and nucleation behavior of Zn^{2+} is predominantly governed by the Zn^{2+} flux at the anode/electrolyte interface. To investigate the impact of ZSL on regulating the Zn^{2+} concentration field, COMSOL Multiphysics simulations were conducted. As illustrated in Figs. 3a and 3b, the concentration gradient of Zn^{2+} from the bulk $ZnSO_4$ electrolyte to the ZSL@Zn anode surface is lower than that on the bare Zn anode, which is conducive to reducing the dendrites induced by concentration polarization [39,40]. Density functional theory (DFT) calculations were also conducted to elucidate the homogeneity of the zinc ion flux on ZSL@Zn. As shown in Fig. 3c, the adsorption energy of Zn^{2+} on ZSL@Zn is higher than that on bare Zn (−0.16 vs. −0.06 eV), indicating its exceptional chemical affinity with Zn^{2+}. A stable zinc ion flux at the interface is of critical importance for the homogeneous deposition of zinc and the inhibition of zinc dendrite formation.

The in-situ Raman spectroscopy was employed to monitor fluctuations in zinc ion concentration at the electrode/electrolyte interface during the zinc deposition process. The Raman signal of the SO_4^{2-} ion at 980 cm^{-1} serves as an indicator of variations in Zn^{2+} ion concentration [41]. In the case of the bare Zn anode, a notable reduction in the Raman signal strength is detected during electroplating, indicative of an elevated concentration polarization of Zn^{2+} ions on the anode surface (Fig. 3d). In contrast, the ZSL@Zn anode exhibits a stable Raman signal throughout the plating process, indicating a consistent and uniform distribution of Zn^{2+} ions at the interface (Fig. 3e). Moreover, the region around 3500 cm^{-1} in the Raman spectra, typically associated with O–H stretching vibrations[39], offers insights into the interaction between water molecules and the zinc surface. During electroplating, the presence of the ZSL layer effectively reduces direct contact between H_2O and the zinc surface, thereby mitigating water consumption within the electrolyte. Consequently, the ZSL@Zn anode maintains a stable Raman signal in this region, whereas the bare Zn anode exhibits a rapid decline, suggesting the enhanced water-induced side reactions.

The simulation of the possible diffusion paths and energy barriers of

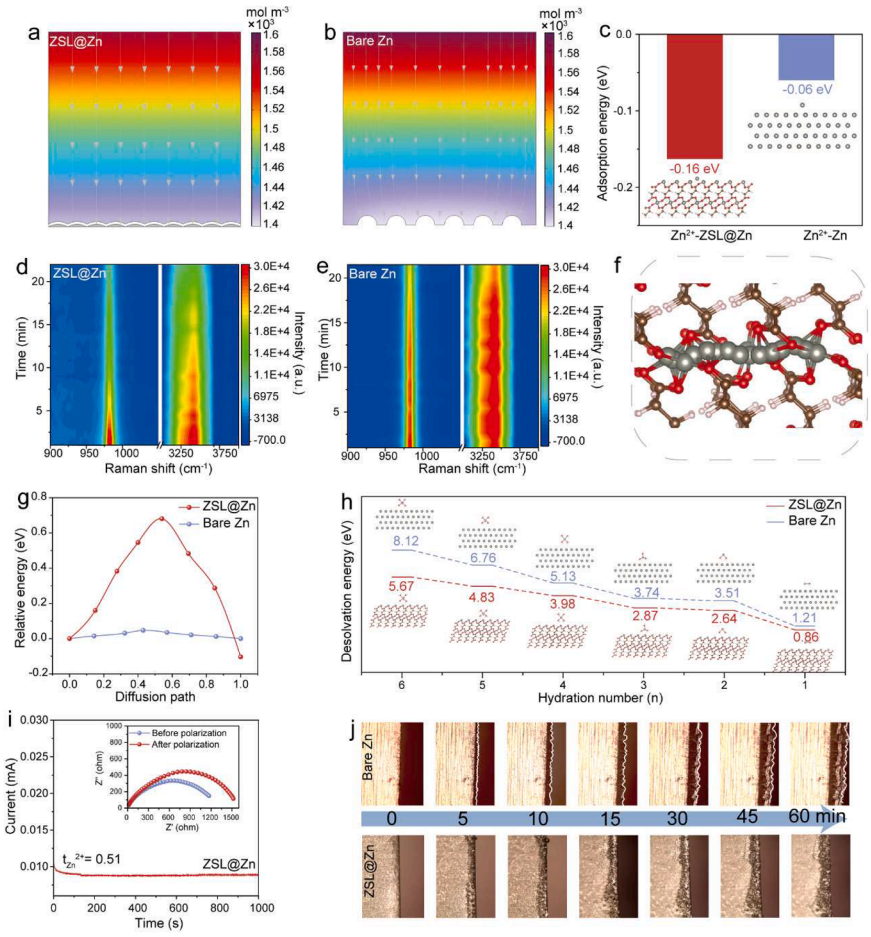

Fig. 3. Zn^{2+} concentration field simulation on (a) ZSL@Zn and (b) bare Zn electrode. (c) Adsorption energy of Zn^{2+} on the surfaces of the bare Zn and ZSL@Zn anodes. In situ Raman spectra of (d) bare Zn and (e) ZSL@Zn anodes at 2 mA·cm^{-2}. (f) The possible migration pathway on ZSL and (g) calculated migration energy barriers of Zn^{2+} along the c-axis. (h) Comparison of energy barriers during the step-by-step de-solvation process of $[Zn(H_2O)_n]^{2+}$. (i) CA curve and the corresponding EIS plots of the ZSL@Zn symmetric cell. (j) In situ optical microscopy images of the Zn deposition process on bare Zn and ZSL@Zn.

Zn^{2+}(Figs. 3f, 3g and S22) shows that the diffusion barrier on the ZSL surface (0.68 eV) is higher than that on the bare Zn surface (0.05 eV), but lower than that on ZHS [42]. A lower diffusion barrier tends to trigger uncontrolled two-dimensional diffusion, resulting in local cluster stacking to form inhomogeneous nuclei and dendrite formation. In contrast, a higher diffusion barrier is not conducive to the rapid Zn^{2+} diffusion, which may cause concentration polarization at high current densities and promote dendrite formation. The activation energy (E_a) for zinc ion migration, which corresponds to the de-solvation energy barrier for hydrated Zn^{2+} ions, was evaluated using temperature-dependent electrochemical impedance spectroscopy (EIS) plots. As depicted in Figure S23, the charge transfer resistance (R_{ct}) values of the ZSL@Zn symmetric cell are consistently lower than those of the bare Zn symmetric cell across the temperature range of 40 to 80 °C. The E_a value of ZSL@Zn, derived from the Arrhenius equation, is lower than that of bare Zn (44.51 vs. 48.84 kJ mol^{-1}) (Figure S24). This lower activation energy suggests an accelerated de-solvation process and reduced concentration polarization at the electrode/electrolyte interface. DFT calculations illustrates that the de-solvation barrier for hydrated Zn ions at the ZSL@Zn/electrolyte interface is lower than that of bare Zn (Fig. 3h), suggesting faster diffusion kinetics. As a result, ZSL@Zn demonstrates a lower nucleation overpotential (NOP) of approximately 60 mV compared to 82 mV for bare Zn, as shown in the cyclic voltammetry (CV) curves (Figure S25). The Zn^{2+} transport capacity in ZSL@Zn was evaluated by measuring the Zn^{2+} transfer number (t_{Zn}^{2+}) using the Bruce-Vincent method. As illustrated in Figs. 3i and S26, the ZSL@Zn electrode has a lower initial impedance and exhibits a smaller impedance change. The Zn^{2+} transfer number of ZSL@Zn is 0.51, significantly higher than that of bare Zn (0.28), indicating a highly selective ionic transfer process.

In addition, the deposition mechanism of Zn on bare Zn and ZSL@Zn electrodes was probed through the chronoamperometry (CA) method, which captures the surface morphology evolution by recording the fluctuation of the current-time curve during the nucleation process. The current intensity of bare Zn consistently increases over 500 s, indicating that the zinc deposition on bare Zn is mainly dominated by two-dimensional lateral diffusion, which is prone to rampant dendrite growth. In sharp contrast, the initial two-dimensional diffusion of zinc ions on ZSL@Zn is primarily detected within 30 s, and stable three-dimensional diffusion is verified in the subsequent process (Figure S27). The morphology of Zn deposition at the electrolyte/anode interface was subsequently monitored utilizing in-situ optical microscopy to highlight the beneficial role of the ZSL in regulating the Zn deposition behavior. Fig. 3j illustrates that after 5 min of deposition, bare Zn surfaces exhibit small irregular protuberances that appear on the bare Zn surface and gradually develop into irregular Zn dendrites during the ongoing plating process. In contrast, the ZSL@Zn surface consistently exhibits a uniform Zn plating layer throughout the deposition process, devoid of noticeable protuberances. This observation underscores ZSL's ability to promote stable and uniform Zn deposition [43].

As previously reported, the relatively smooth surface and uniform

interfacial charge density of the Zn (002) plane make the dendrite growth more challenging than on other planes [44–46]. In addition, the Zn (002) plane has the lowest surface energy and electrochemical activity, which help alleviate corrosion and mitigate H_2 emission and by-product generation [47]. Therefore, enhancing the deposition along the (002) plane is crucial to maximize these advantages. However, factors such as slow de-solvation of hydrated Zn^{2+}, inhomogeneous Zn^{2+} flux distribution, strong concentration polarization, and poor Zn^{2+} transport kinetics induced by-products practically impede the preferential growth of Zn (002) planes. DFT calculations were used to evaluate the impact of ZSL on the surface energy of the Zn (002) plane. As shown in Fig. 4a, the introduction of ZSL reduces the surface energy of Zn (002) to 0.27 J m^{-2}, significantly lower than the 0.68 J m^{-2} of pure Zn. In addition, ZSL accelerates the de-solvation process and enhances the Zn^{2+} transport kinetics, thus ultimately promoting the deposition of Zn^{2+} along the (002) plane. This is further supported by the $I_{(002)}/I_{(101)}$ ratio, which compares the intensity of the diffraction peaks of the (002) and (101) planes during the electroplating and cycling. As depicted in Fig. 4b, during the initial plating process, the $I_{(002)}/I_{(101)}$ ratio of the ZSL@Zn electrode gradually increases with the plating time. At the end of electroplating, the ratio increases significantly to 1.75, significantly higher than 0.92 for bare Zn (Fig. 4c), indicating that ZSL promotes the preferential orientation of the Zn (002) crystal surface. After various subsequent cycles, the $I_{(002)}/I_{(101)}$ values of ZSL@Zn are consistently higher than those of bare Zn (Figure S28), further demonstrating the long-lasting effect of ZSL in regulating crystal deposition.

To evaluate the stability of the ZSL interfacial layer during cycling, the ZSL@Zn electrode was analyzed after being extracted from disassembled symmetrical cells following 20 cycles at 1 mA cm^{-2} and 1 mAh cm^{-2}. The FTIR spectrum of the ZSL@Zn electrode reveals characteristic vibrational peaks at 1540 and 1389 cm^{-1} (Figure S29), aligning with those of zinc succinate powder. SEM images show that irregular holes appear on the bare Zn surface, which is not conducive to uniform Zn deposition and easily induces dendrite growth, resulting in cell short-circuit (Figure S30). In contrast, ZSL@Zn electrodes remain in their original armor-like structure without protrusions after cycling (Fig. 4d). This indicates that the interfacial layer remains intact after extensive Zn plating/stripping cycles. XRD results further identify the presence of distinct peaks of the passivation by-product ZHS in the cycled bare Zn, which is invisible in ZSL@Zn (Figure S31). This is due to the fact that the tight bond between the interfacial protective layer and the zinc foil effectively blocks the direct contact between water molecules and the zinc foil, which attenuates the emergence of by-products. In addition, the electrical impedance plots of bare Zn and ZSL@Zn symmetric cells were recorded after various cycles, and it was found that the charge transfer resistance (R_{ct}) of both gradually decreases in the initial 5 cycles, with the R_{ct} of the bare Zn symmetric cell always being larger (Figure S32). However, after 20 cycles, the resistance of the bare zinc symmetric cell starts to increase, which mainly stems from the electrolyte degradation and the massive formation of ZHS. Conversely, the resistance of the symmetric cell with ZSL@Zn is still decreasing and shows favorable stability. Further validation comes from the XPS depth results in conjunction with Ar^+ sputtering, which confirms the persistence of the interfacial layer. As illustrated in Fig. 4e, O—*C* = *O* (288.7

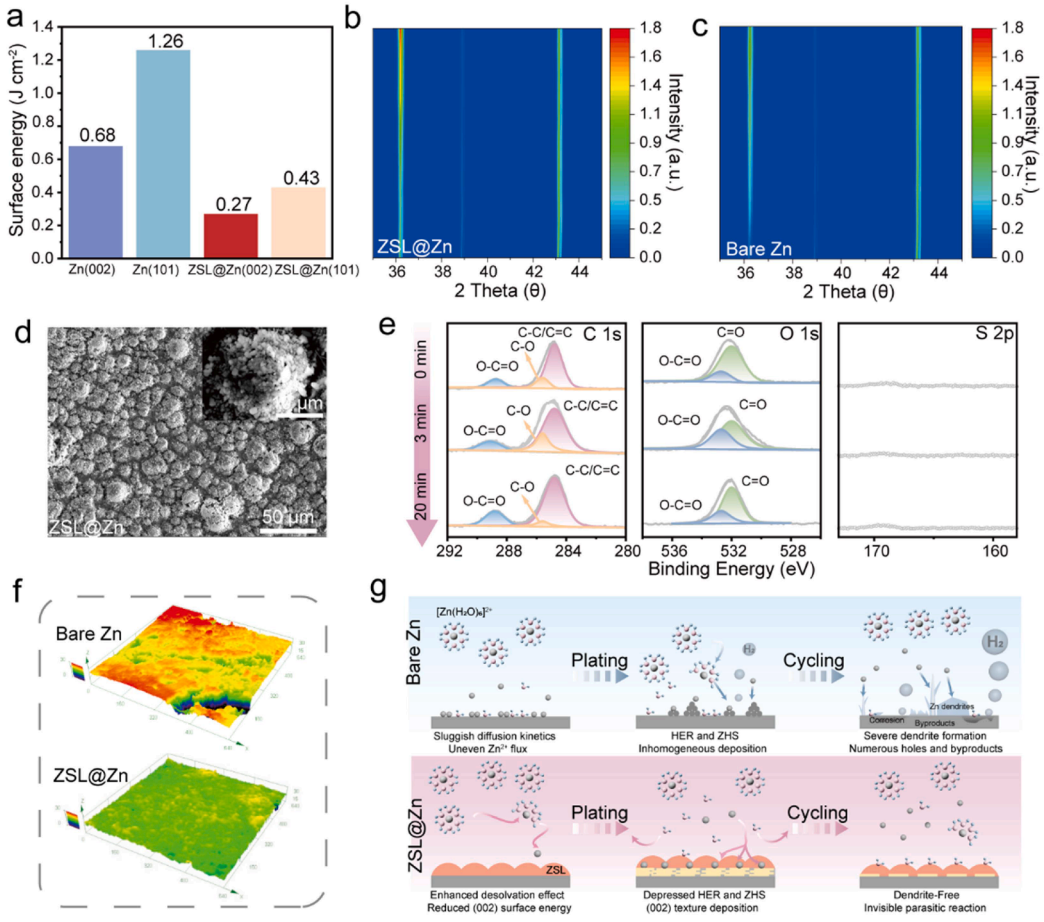

Fig. 4. (a) Surface energy of (002), (101) crystal planes for bare Zn and ZSL@Zn anodes. In situ XRD characterizations of (b) ZSL@Zn and (c) bare Zn anodes plating at 8.85 mA·cm^{-2}. (d) SEM images of ZSL@Zn after cycling. (e) XPS depth profiles of C 1 s, O 1 s, and S 2p for the post-cycling ZSL@Zn anode at different Ar^+ sputtering time. (f) Confocal laser scanning microscope images of bare Zn and ZSL@Zn anodes following 50 cycles at 1 mA cm^{-2}. (g) Schematic illustration of zinc deposition behavior and interfacial interaction of bare Zn and ZSL@Zn anodes.

eV), C—O (285.6 eV), and C—C/*C* = *C* (284.8 eV) peaks are observed in the C 1 s spectra before sputtering, which is similar to the chemical composition of ZSL. Also, the peak density of O—*C* = *O* gradually expands with the increase of sputtering time, which further verifies the excellent mechanical durability and chemical stability of ZSL during repeated plating/stripping processes. In addition, the S 2p spectra exhibit no signals of SO_4^{2-} (169.7 eV), SO_3^{2-} (168.6 eV), and ZnS (162.0 eV), which are detected on the bare Zn surface after cycling (Figure S33). The SO_4^{2-} signal originates from ZHS, while the latter two are decomposition products of $ZnSO_4$ salt. To elucidate the modulation effect of Zn deposition by ZSL, the anodes was subjected to 50 cycles at 1 mA cm^{-2}, followed by analysis using the confocal laser scanning microscope (CLSM) (Fig. 4f). The bare Zn anode displays an uneven surface with noticeable holes and dendrite growth, while the ZSL@Zn anode maintained a smooth surface, indicating uniform Zn deposition and suppressed side reactions. The above results indicate that bare Zn is highly susceptible to severe dendrite growth and rampant parasitic reactions due to the thermodynamic instability of Zn. The in-situ constructed ZSL delivers abundant active sites to effectively adsorb Zn ions, promotes the rapid de-solvation of $[Zn(H_2O)_6]^{2+}$, and enhances the diffusion/deposition kinetics, thus ensuring homogeneous ionic flux and reduced concentration polarization. Encouragingly, the ZSL, firmly anchored to the Zn anode, effectively reduces the surface energy and facilitates the preferential growth of the Zn (002) plane. Finally, the three-dimensional network in ZSL can effectively capture the active water and inhibit the parasitic reaction (Fig. 4 g).

2.3. Electrochemical performance of ZSL@Zn anodes

The Coulombic efficiency (CE) is an indispensable parameter to assess the plating/stripping reversibility of zinc metal anodes. Therefore, the asymmetric cells comprising of ZSL@Zn or bare anodes were used to reveal the cycling efficiency in 2 M $ZnSO_4$ electrolytes. The CE of the bare Zn||Cu asymmetric cell decays rapidly to a short circuit caused by the dendrite growth and serious parasitic reactions after 204 cycles. In contrast, the asymmetric cells with ZSL@Zn anodes deliver a stable plating/stripping process for 6000 cycles with an impressive average CE of 99.89 %, which is attributed to the dendrite-free plating process with the assistance of the interfacial layer (Fig. 5a). Interestingly, even though the copper foil is bare, the nucleation overpotential of ZSL@Zn||Cu is substantially lower than that of bare Zn||Cu (Figure S34), suggesting that ZSL contributes to the homogeneous transport of the Zn ions and induces smaller nucleation. This is also confirmed by the morphology of bare Zn and ZSL@Zn plated to bare Cu. The deposits

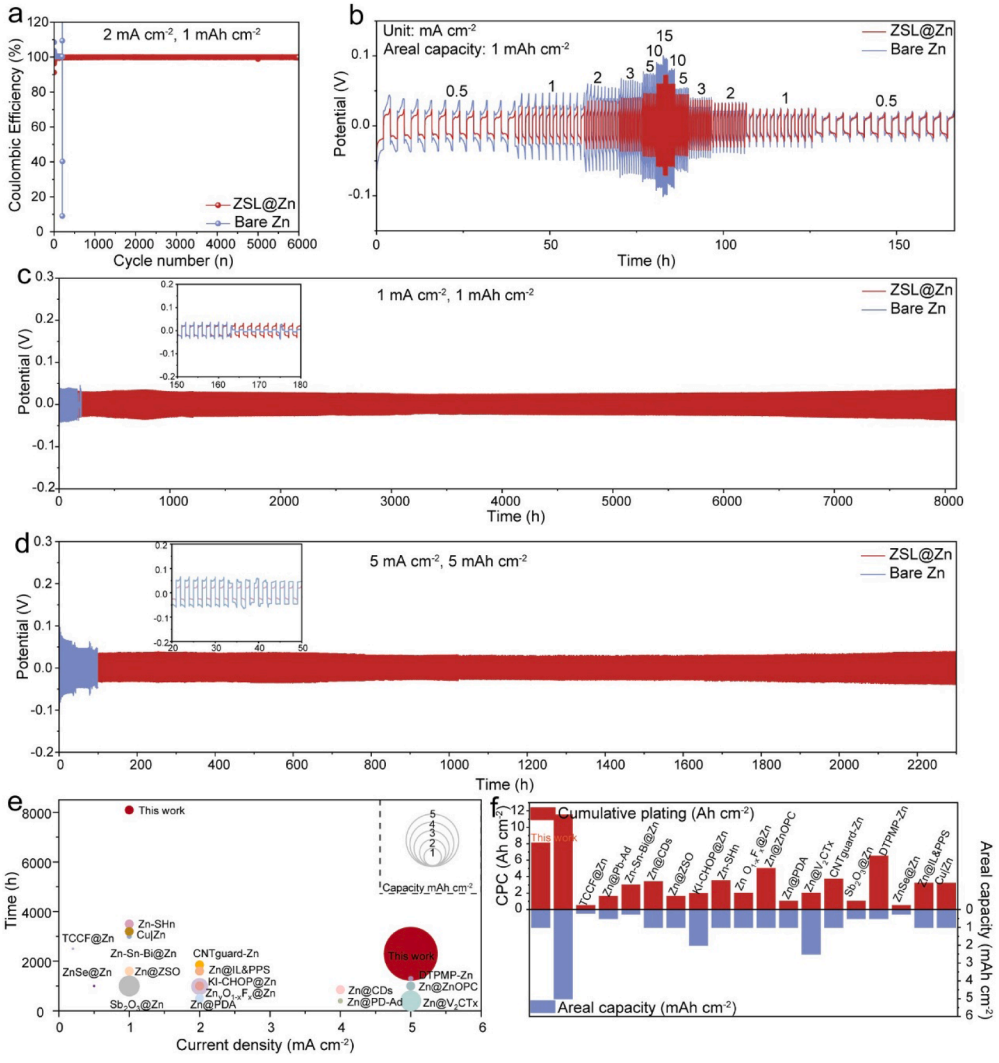

Fig. 5. (a) CE profiles of Zn plating and striping in bare Zn||Cu and ZSL@Zn||Cu asymmetrical cells. (b) Rate performance of symmetric cells with different anodes at various current densities. Galvanostatic cycling performance of ZSL@Zn and bare Zn symmetrical cells at (c) 1 mA cm^{-2}, 1 mAh cm^{-2} and (d) 5 mA cm^{-2}, 5 mAh cm^{-2}, respectively. (e) The longevity comparison of the ZSL@Zn anode with previously documented modified Zn anodes (inset: circle sizes indicate testing capacities). (f) Cumulative capacity and areal capacity comparison between ZSL@Zn and recently modified Zn anodes.

plated on the Cu surface of the asymmetric cell with bare Zn present variable sizes and random stacking, which readily stimulates the Zn dendrite growth. In contrast, the surfaces plated on the Cu surface in the ZSL@Zn||Cu cell are flat and ordered with no visible dendrite generation (Figure S35). Furthermore, the ZSL@Zn||Cu cell exhibits stable galvanostatic plating/stripping profiles with a lower polarization voltage gap than the bare Zn||Cu asymmetric cell (Figure S36), indicating its lower energy barriers of nucleation and dissolution. This result underscores that the in situ-formed ZSL ensures uniform zinc deposition and enhances the reversibility and stability of the zinc anode.

Besides CE, the rate performance of bare Zn and ZSL@Zn symmetric cells was also recorded by cycling under various current densities (Fig. 5b). Apparently, the hysteresis voltages of bare Zn are substantially larger than those of ZSL@Zn, suggesting that the hydrophilic ZSL accelerates Zn^{2+} transfer and enhances Zn plating/stripping kinetics. This is further corroborated by the exchange current density for the Zn electrodeposition process (Figure S37). To evaluate the cycling stability of ZSL@Zn electrodes, the galvanostatic cycling performance of symmetric cells was recorded at various current densities and capacities. As illustrated in Fig. 5c, the bare Zn electrode experiences an abrupt voltage plunge after merely 163 h at 1 mA cm^{-2} with a fixed capacity of 1 mAh cm^{-2}, which is probably triggered by dynamic dendrites during the repeated plating/stripping process. In contrast, the symmetric cell with ZSL@Zn features a stable and tiny hysteresis voltage (≈71 mV) and an exceptionally prolonged cycle life of >8000 h, which is 49 times longer than that of the bare Zn anode. Impressively, as the current is increased to 5 mA cm^{-2} and the capacity is extended to 5 mA h cm^{-2}, the ZSL@Zn symmetric cell consistently remains excellent stability, accompanied by almost no obvious voltage fluctuation for 2300 h, whereas the bare Zn||Zn cells suffer short-circuit failure after 32 h (Fig. 5d). Even at a high depth of discharge (DoD) value of up to 43.4 %, the ZSL@Zn symmetric cell still demonstrates a steady lifetime of over 700 h (Figure S38). Furthermore, the cycling performance of zinc foils treated with different concentrations of SA-MeOH solution and binary carboxylic acids with various carbon chains were also evaluated. As expected, the properties of zinc foils treated with different concentrations of SA-MeOH solutions and binary carboxylic acids are superior to those of bare zinc (Figures S39 and S40). Apparently, Zn symmetrical cells treated with binary carboxylic acids containing four to six carbon atoms demonstrate the substantially preferable cycling life. This may be attributed to the fact that binary carboxylic acids with suitable carbon chains promote the growth of a homogeneous and dense interfacial layer on the Zn surface and exhibit proper zincophilic features, which reduce the formation of dendrites and enhance the overall stability of the zinc anode. In addition, the incorporation of succinic acid as an additive to the electrolyte also allows the zinc anode to exhibit remarkable cycling stability and reversibility (Figure S41). Overall, this work exhibits positive competitiveness in terms of both cycle life and cumulative capacity at the same current density and constant capacity compared to the recently reported high-performance Zn anodes, as presented in Figs. 5e, 5f and Table S1[43,48–61].

To further validate the superiority of the ZSL@Zn electrode, the ZSL@Zn electrode was paired with $Na_2V_6O_{16}·3H_2O$ (NVO) cathode materials and assembled into full cells. NVO cathodes were prepared by a hydrothermal method according to previous reports[62], which exhibit a nanorod-like shape in Figure S42a. All the XRD diffraction peaks of the cathode coincide with $Na_2V_6O_{16}·3H_2O$ (JCPDS 16–0601), further evidencing the high purity of the as-prepared cathode (Figure S42b). Fig. 6a illustrates the comparative cyclic voltammogram (CV) curves of full cells employing bare Zn and ZSL@Zn anodes, both of which have similar redox peaks, suggesting that the protective layer has no noticeable impact on the electrochemical behaviors of ZIBs. The larger CV closure area and smaller voltage gap reveal the favorable influence of ZSL on the rapid Zn^{2+} transport kinetics. This was verified by the following rate performance of the full cell (Fig. 6b). With a high loading mass of up to 6.5 mg cm^{-2}, the specific capacity of the ZSL@Zn full cell could still be preserved at 179.7 mAh g^{-1} at high current density and then recovered to 312.6 mAh g^{-1} at 0.2 A g^{-1}. In contrast, the comparable capacity of the full cell with bare zinc is lower than that of ZSL@Zn as expected. The superior performance of the ZSL@Zn full cell at high current densities implies its fast electron/ion transport, which can be verified by its low charge transfer and diffusion impedance in the

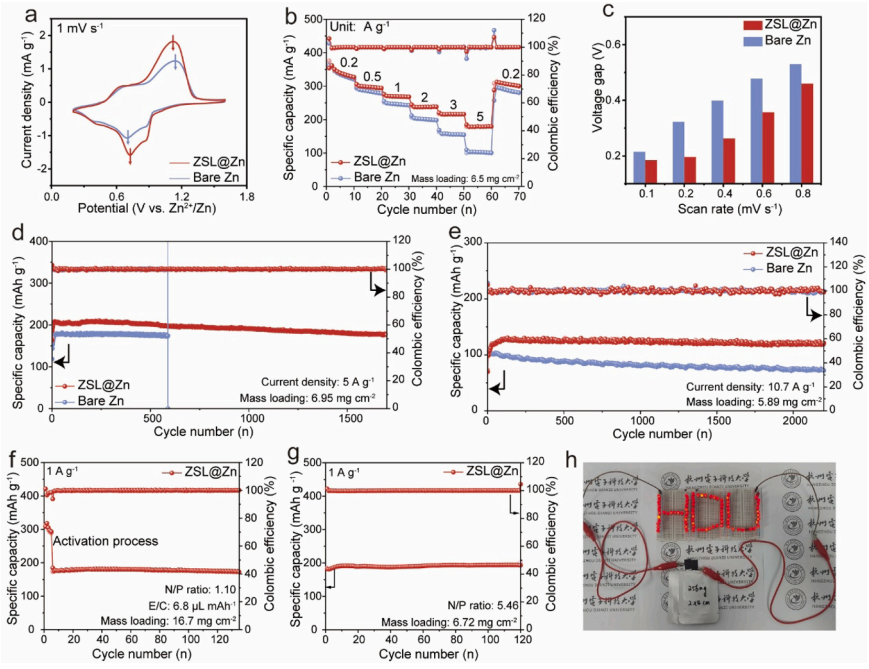

Fig. 6. (a) CV curves at 1 mV s^{-1}, and (b) rate performance of ZSL@Zn||NVO and bare Zn||NVO full cells. (c) Voltage gap between the redox peaks for ZSL@Zn||NVO and bare Zn||NVO cells after rate test. Long-term cycling performance and Coulombic efficiencies of ZSL@Zn||NVO and bare Zn||NVO full cells at (d) 5 A g^{-1} and (e) 10.7 A g^{-1}, respectively. (f) Cycling performance of ZSL@Zn||NVO full cell under harsh conditions (an activation process conducted at 0.1 A g^{-1} for the initial 5 cycles). (g) Cycling performance of ZSL@Zn||NVO pouch cell at 1 A g^{-1}. (h) Photograph of the pouch cells powering the LED lights.

EIS and DRT analysis results (Figure S43). The galvanostatic charge/-discharge (GCD) profiles similarly reveal a smaller voltage polarization for ZSL@Zn than bare Zn (Figure S44), which is consistent with the above CV curves. As illustrated in Figure S45, the electrochemical behavior of the ZSL@Zn||NVO full cell was further evaluated using cyclic voltammetry (CV) across various scan rates. All the CV curves demonstrate distinct redox peaks, indicative of efficient and reversible charge transfer processes over scan rates. Fig. 6c presents a comparative analysis of the voltage gap between the redox peaks for full cells with different anodes. Notably, the ZSL@Zn||NVO cell exhibits substantially reduced voltage gaps at all scan rates, with a notable improvement at higher sweep speeds. This reduction in voltage gap highlights the enhanced electrochemical kinetics and diminished polarization associated with the ZSL@Zn anode compared to the bare Zn anode.

In addition, the long-term cycling performance of the ZSL@Zn full cell was evaluated at different current densities (5 and 10.7 A g^{-1}), respectively. After 1700 cycles, the capacity of the ZSL@Zn full cell remains as high as 177.5 mAh g^{-1} at 5 A g^{-1} (Fig. 6d). In contrast, the bare Zn cell failed instantly after 588 cycles, accompanied by a continual reduction in capacity. The low-capacity retention and quick failure of the bare Zn cell are mainly ascribed to severe electrochemical corrosion and disordered accumulation of dendrites. The high capacity of 119.8 mAh g^{-1} is still sustained for ZSL@Zn||NaVO full cells after 2200 cycles when the current density is raised to 10.7 A g^{-1} with an amazing capacity retention and an average CE of 99.33 % (Fig. 6e). Notably, to verify the feasibility of its practical application, the cycling performance of the ZSL@Zn||NVO full cell was subsequently investigated under rigorous conditions, where the thickness of zinc foil used was 10 um with the mass loading of NVO cathode materials at 16.7 mg cm^{-2}, an electrolyte-to-capacity (E/C) ratio of 6.8 μL mAh^{-1} and a N/P ratio of 1.10. As depicted in Fig. 6f, the specific capacity of the full cell exhibits exceptional stability following an initial five-cycle activation process at a current density of 1 A g^{-1}, maintaining 174.2 mAh g^{-1} after 130 cycles with a high CE of 99.94 %.

Following the outstanding performance of the ZSL@Zn anode demonstrated in coin cells, it was subsequently validated in pouch cells (Fig. 6g). These series-connected pouch cells effectively power LEDs, as seen in Figs. 6h and S46. Remarkably, despite undergoing folds at various angles (0°, 90°, and 180°) and several folds, the pouch cells maintain their ability to power the LEDs without any alteration in the open-circuit voltage, demonstrating the outstanding flexibility of the ZSL@Zn anode. To further ascertain its safety for practical use, the pouch cells underwent rigorous testing, including cutting. Notwithstanding these severe circumstances, they continually power the LEDs without short-circuit or explosion, demonstrating a remarkable level of stability and safety (Figure S47). These impressive results emphasize the revolutionary potential of the ZSL artificial layer in improving the development of practical and dependable battery designs.

3. Conclusions

In this work, we have significantly improved the plating/stripping reversibility and resistance to side reactions of zinc anodes by constructing an in-situ armor-like interfacial layer (ZSL). This robust ZSL, enriched with zincophilic carboxyl groups of electron donors, facilitates the homogeneous distribution of Zn^{2+} flux, reduces the migration energy barrier, and accelerates the de-solvation process to boost the deposition kinetics. Additionally, the ZSL regulates the interfacial pH, effectively capturing reactive water molecules and mitigating parasitic side reactions. Notably, the zinc succinate coordination polymer drastically reduces the surface energy of zinc anodes and promotes the preferential orientation of Zn (002) planes. When applied in symmetrical cells, this interfacial layer delivers exceptional long-term cycling stability, lasting up to 8000 h at 1 mA cm^{-2} and 1 mAh cm^{-2}, with low polarization voltage and an average coulombic efficiency of 99.89 % over 6000 cycles. In full cells with $Na_2V_6O_{16}{\cdot}3H_2O$ cathodes, the system exhibits remarkable rate performance and cycling stability. These results emphasize the potential of in-situ interfacial layers in enhancing the electrochemical performance and longevity of zinc anodes for aqueous zinc-ion batteries through the synergistic effects of Zn^{2+} homogenization regulation and water molecule separation.

Data availability

Data will be made available on request.

CRediT authorship contribution statement

Tao Yang: Visualization, Writing – original draft, Investigation, Writing – review & editing, Conceptualization. **Tianyu Shen:** Writing – original draft, Writing – review & editing, Investigation, Conceptualization. **Yuhang Liang:** Software, Writing – review & editing, Investigation, Data curation, Formal analysis. **Miaojie Fang:** Writing – review & editing, Data curation, Investigation. **Hongbo Wu:** Data curation, Investigation, Writing – review & editing. **Ouwei Sheng:** Investigation, Writing – review & editing, Formal analysis, Data curation. **Hongli Chen:** Investigation, Writing – review & editing. **Chang Dong:** Writing – review & editing, Data curation. **Haojie Ji:** Investigation, Writing – review & editing. **Jian Zhang:** Writing – review & editing, Data curation. **Rongkun Zheng:** Data curation, Resources, Supervision. **Hao Liu:** Writing – review & editing, Supervision, Formal analysis. **Guoxiu Wang:** Formal analysis, Supervision, Writing – review & editing. **Xuefeng Zhang:** Resources, Supervision, Project administration, Writing – review & editing.

Declaration of competing interest

The authors declare the following financial interests/personal relationships which may be considered as potential competing interests: Xuefeng Zhang reports financial support was provided by National Science Fund for Distinguished Young Scholars. Tao Yang reports financial support was provided by Natural Science Foundation of Zhejiang Province. Ouwei Sheng reports financial support was provided by National Natural Science Foundation of China. Guoxiu Wang reports financial support was provided by Australian Research Council. If there are other authors, they declare that they have no known competing financial interests or personal relationships that could have appeared to influence the work reported in this paper.

Acknowledgments

We acknowledge financial support from the National Science Fund for Distinguished Young Scholars (No. 52225312), the Natural Science Foundation of Zhejiang Province (No. LMS25E020002, LY24B030008), and the National Natural Science Foundation of China (No. 52002101, 22209032). The theoretical work was supported by computational resources provided by the Australian Government through Gadi under the National Computational Merit Allocation Scheme and was accessed through the SIH HPC Allocation Scheme [LE190100021]. Authors would like to thank the support provided by the Australian Research Council through the ARC Discovery project (DP230101579).

Supplementary materials

Supplementary material associated with this article can be found, in the online version, at doi:10.1016/j.ensm.2025.104411.

References

[1] Q. Kang, Z. Zhuang, Y. Liu, Z. Liu, Y. Li, B. Sun, F. Pei, H. Zhu, H. Li, P. Li, et al., Engineering the Structural Uniformity of Gel Polymer Electrolytes via Pattern-guided Alignment for Durable, Safe Solid-state Lithium Metal Batteries, Adv. Mater. 35 (38) (2023) 2303460, https://doi.org/10.1002/adma.202303460.

[2] A.L. Lipson, R.S. Ginder, M.C. Hersam, Nanoscale in situ characterization of Li-ion battery electrochemistry via scanning ion conductance microscopy, Adv. Mater. 23 (47) (2011) 5613–5617, https://doi.org/10.1002/adma.201103094.

[3] Q. Hu, J. Hou, Y. Liu, L. Li, Q. Ran, J. Mao, X. Liu, J. Zhao, H. Pang, Modulating zinc metal reversibility by confined antifluctuator film for durable and dendrite-free zinc ion batteries, Adv. Mater. 35 (36) (2023) 2303336, https://doi.org/10.1002/adma.202303336.

[4] M. Zhao, Y. Lv, S. Zhao, Y. Xiao, J. Niu, Q. Yang, J. Qiu, F. Wang, S. Chen, Simultaneously Stabilizing both Electrodes and Electrolytes by a Self-Separating Organometallics Interface for High Performance Zinc-Ion Battery at Wide Temperatures, Adv. Mater. 34 (49) (2022) 2206239, https://doi.org/10.1002/adma.202206239.

[5] G. Zhang, H. Gao, D. Zhang, J. Xiao, L. Sun, J. Li, C. Li, Y. Sun, X. Yuan, P. Huang, et al., Transformative Catalytic Carbon Conversion Enabling Superior Graphitization and Nanopore Engineering in Hard Carbon Anodes for Sodium-Ion Batteries, Carbon Energy (2025), https://doi.org/10.1002/cey2.713.

[6] J. Xiao, H. Gao, Y. Xiao, S. Wang, C. Gong, Z. Huang, B. Sun, C.-L. Dong, X. Guo, H. Liu, et al., A hydro-stable and phase-transition-free P2-type cathode with superior cycling stability for high-voltage sodium-ion batteries, Chem. Eng. J. 506 (2025) 160010, https://doi.org/10.1016/j.cej.2025.160010.

[7] Q. Jiao, X. Zhai, Z. Sun, W. Wang, S. Liu, H. Ding, W. Chu, M. Zhou, C. Wu, Ultrafast Super-filling Construction of Metal Artificial Interface for Long-term Stable Zinc Anode, Adv. Mater. 35 (29) (2023) 2300850, https://doi.org/10.1002/adma.202300850.

[8] Z. Hou, T. Zhang, X. Liu, Z. Xu, J. Liu, W. Zhou, Y. Qian, H.J. Fan, D. Chao, D. Zhao, A solid-to-solid metallic conversion electrochemistry toward 91 % zinc utilization for sustainable aqueous batteries, Sci. Adv. 8 (41) (2022) 1, https://doi.org/10.1126/sciadv.abp8960.

[9] D. Wang, H. Liu, D. Lv, C. Wang, J. Yang, Y. Qian, Rational Screening of Artificial Solid Electrolyte Interphases on Zn for Ultrahigh-Rate and Long-Life Aqueous Batteries, Adv. Mater. 35 (2) (2022) 2207908, https://doi.org/10.1002/adma.202207908.

[10] M. Liu, W. Yuan, G. Ma, K. Qiu, X. Nie, Y. Liu, S. Shen, N. Zhang, In-Situ Integration of a Hydrophobic and Fast-Zn^{2+}-Conductive Inorganic Interphase to Stabilize Zn Metal Anodes, Angew. Chem.Int. Edit. 62 (27) (2023) e202304444, https://doi.org/10.1002/anie.202304444.

[11] Z. Liu, G. Li, M. Xi, Y. Huang, H. Li, H. Jin, J. Ding, S. Zhang, C. Zhang, Z. Guo, Interfacial engineering of Zn metal via a localized conjugated layer for highly reversible aqueous zinc ion battery, Angew. Chem. Int. Ed. Engl. 63 (14) (2024) 202319091, https://doi.org/10.1002/anie.202319091.

[12] X. Wang, W. Zhou, L. Wang, Y. Zhang, S. Li, X. Li, Z. Zhao, T. Zhang, H. Jin, X. Song, et al., Benchmarking corrosion with anionic polarity index for stable and fast aqueous batteries even in low-concentration electrolyte, Adv. Mater. 37 (14) (2025) e2501049, https://doi.org/10.1002/adma.202501049.

[13] Z. Xing, Y. Sun, X. Xie, Y. Tang, G. Xu, J. Han, B. Lu, S. Liang, G. Chen, J. Zhou, Zincophilic electrode interphase with appended proton reservoir ability stabilizes Zn metal anodes, Angew. Chem.Int. Edit. 62 (5) (2022) e202215324, https://doi.org/10.1002/anie.202215324.

[14] H. Du, R. Zhao, Y. Yang, Z. Liu, L. Qie, Y. Huang, High-capacity and long-life zinc electrodeposition enabled by a self-healable and desolvation shield for aqueous zinc-ion batteries, Angew. Chem.Int. Edit. 61 (10) (2022) e202114789, https://doi.org/10.1002/anie.202114789.

[15] D. Li, L. Cao, T. Deng, S. Liu, C. Wang, Design of a solid electrolyte interphase for aqueous Zn batteries, Angew. Chem.Int. Edit. 60 (23) (2021) 13035–13041, https://doi.org/10.1002/anie.202103390.

[16] P. Wang, S. Liang, C. Chen, X. Xie, J. Chen, Z. Liu, Y. Tang, B. Lu, J. Zhou, Spontaneous Construction of Nucleophilic Carbonyl-Containing Interphase towards Ultra-Stable Zinc Metal Anodes, Adv. Mater. 34 (33) (2022) 2202733, https://doi.org/10.1002/adma.202202733.

[17] X. Cai, X. Wang, Z. Bie, Z. Jiao, Y. Li, W. Yan, H.J. Fan, W. Song, A Layer-by-layer self-assembled biomacromolecule film for stable zinc anode, Adv. Mater. 36 (3) (2023) 2306734, https://doi.org/10.1002/adma.202306734.

[18] M. Fang, T. Yang, O. Sheng, T. Shen, Z. Huang, R. Zheng, C. Zhang, J. Zhang, X. Zhang, A trinity strategy enabled by iodine-loaded nitrogen-boron-doped carbon protective layer for dendrite-free zinc-ion batteries, J. Colloid Interface Sci. 661 (2024) 987–999, https://doi.org/10.1016/j.jcis.2024.02.053.

[19] L. Sun, X. Cao, L. Gao, J. Li, C. Qian, J. Wu, X. Nie, H. Gao, P. Huang, Y. Zhao, et al., Immobilizing Zwitterionic Molecular Brush in Functional Organic Interfacial Layers for Ultra-Stable Zn-Ion Batteries, Nanomicro Lett 17 (1) (2025) 262, https://doi.org/10.1007/s40820-025-01782-5.

[20] Y. Liu, S. Zheng, J. Ma, X. Wang, L. Zhang, P. Das, K. Wang, Z.S. Wu, All 3D Printing Shape-Conformable Zinc Ion Hybrid Capacitors with Ultrahigh Areal Capacitance and Improved Cycle Life, Adv. Energy Mater. 12 (27) (2022) 2200341, https://doi.org/10.1002/aenm.202200341.

[21] Q. Cao, H. Gao, Y. Gao, J. Yang, C. Li, J. Pu, J. Du, J. Yang, D. Cai, Z. Pan, et al., Regulating dendrite-free zinc deposition by 3d Zincopilic nitrogen-doped vertical graphene for high-performance flexible Zn-Ion batteries, Adv. Funct. Mater. 31 (37) (2021) 2103922, https://doi.org/10.1002/adfm.202103922.

[22] J. Cao, D. Zhang, C. Gu, X. Wang, S. Wang, X. Zhang, J. Qin, Z.S. Wu, Manipulating crystallographic orientation of zinc deposition for dendrite-free zinc ion batteries, Adv. Energy Mater. 11 (29) (2021) 2101299, https://doi.org/10.1002/aenm.202101299.

[23] Y. Fang, X. Xie, B. Zhang, Y. Chai, B. Lu, M. Liu, J. Zhou, S. Liang, Regulating zinc deposition behaviors by the conditioner of PAN separator for zinc-ion batteries, Adv. Funct. Mater. 32 (14) (2021) 2109671, https://doi.org/10.1002/adfm.202109671.

[24] L. Liu, H. Lu, C. Han, X. Chen, S. Liu, J. Zhang, X. Chen, X. Wang, R. Wang, J. Xu, et al., Salt anion amphiphilicity-activated electrolyte cosolvent selection strategy toward durable Zn metal anode, ACS Nano 17 (22) (2023) 23065–23078, https://doi.org/10.1021/acsnano.3c08716.

[25] T. Wei, Y. Ren, Y. Wang, L. Mo, Z. Li, H. Zhang, L. Hu, G. Cao, Addition of dioxane in electrolyte promotes (002)-textured zinc growth and suppressed side reactions in zinc-ion batteries, ACS Nano 17 (4) (2023) 3765–3775, https://doi.org/10.1021/acsnano.2c11516.

[26] H. Ji, Y. Liang, T. Yang, H. Wu, O. Sheng, T. Shen, C. Dong, T. Du, L. Yin, J. Zhang, et al., Dense solid electrolyte interphase and Zn (002) plane texture enabling high depth-of-discharge anode for highly reversible zinc ion batteries, J. Mater. Sci. Technol. 240 (2026) 56–64, https://doi.org/10.1016/j.jmst.2025.03.055.

[27] T. Wang, C. Li, X. Xie, B. Lu, Z. He, S. Liang, J. Zhou, Anode materials for aqueous zinc ion batteries: mechanisms, properties, and perspectives, ACS Nano 14 (12) (2020) 16321–16347, https://doi.org/10.1021/acsnano.0c07041.

[28] T. Shen, M. Fang, T. Lv, H. Wu, O. Sheng, T. Yang, C. Dong, H. Ji, E. Zhang, X. Zhang, et al., In Situ assembly of metal-organic coordination polymer layers enables highly reversible zn anodes with a long cycle life of over 6900 h, Adv. Funct. Mater. (2024) 2408578, https://doi.org/10.1002/adfm.202408578.

[29] J.-H. Wang, L.-F. Chen, W.-X. Dong, K. Zhang, Y.-F. Qu, J.-W. Qian, S.-H. Yu, Three-dimensional zinc-seeded carbon nanofiber architectures as lightweight and flexible hosts for a highly reversible zinc metal anode, ACS Nano 17 (19) (2023) 23065–23078, https://doi.org/10.1021/acsnano.3c04996.

[30] T. Wang, Y. Tang, M. Yu, B. Lu, X. Zhang, J. Zhou, Spirally grown zinc-cobalt alloy layer enables highly reversible zinc metal anodes, Adv. Funct. Mater. 33 (51) (2023) 2306101, https://doi.org/10.1002/adfm.202306101.

[31] M.E. Pam, D. Yan, J. Yu, D. Fang, L. Guo, X.L. Li, T.C. Li, X. Lu, L.K. Ang, R. Amal, et al., Microstructural engineering of cathode materials for advanced zinc-ion aqueous batteries, Adv. Sci. 8 (1) (2020) 2002722, https://doi.org/10.1002/advs.202002722.

[32] P. Liu, J. Guo, X. Chen, T. Wang, Y. Huang, S. Gao, T. Wang, D. Wu, K. Liu, A zincophilic molecular brush for a dendrite-free, corrosion-resistant, zinc metal anode with a long life cycle, Nano Res 17 (2024) 390–396, https://doi.org/10.1007/s12274-023-6290-x.

[33] H. Yu, Y. Chen, H. Wang, X. Ni, W. Wei, X. Ji, L. Chen, Engineering multi-functionalized molecular skeleton layer for dendrite-free and durable zinc batteries, Nano Energy 99 (2022) 107426, https://doi.org/10.1016/j.nanoen.2022.107426.

[34] C. Zhou, L. Shan, Q. Nan, J. Zhang, Z. Fan, B. Tang, J. Li, J. Yang, H. Zhang, Z. Kang, et al., Construction of robust organic–inorganic interface layer for dendrite-free and durable zinc metal anode, Adv. Funct. Mater. 34 (19) (2024) 2312696, https://doi.org/10.1002/adfm.202312696.

[35] Y. Zhu, Z. Huang, M. Zheng, H. Chen, S. Qian, C. Sun, Y. Tian, Z. Wu, C. Lai, S. Zhang, et al., Scalable construction of multifunctional protection layer with low-cost water glass for robust and high-performance zinc anode, Adv. Funct. Mater. 34 (3) (2023) 2306085, https://doi.org/10.1002/adfm.202306085.

[36] Z. Liu, X. Li, Z. Li, L. Ma, Y. Wang, C. Ye, M. Ye, J. Shen, Stable dendrite-free Zn anode with Janus MXene-Ag interfacial bifunctional protective layer for aqueous zinc-ion batteries, Chem. Eng. J. 479 (1) (2024) 147412, https://doi.org/10.1016/j.cej.2023.147412.

[37] Y. Ding, L. Yin, T. Du, Y. Wang, Z. He, J.A. Yuwono, G. Li, J. Liu, S. Zhang, T. Yang, et al., A Trifunctional electrolyte enables aqueous zinc ion batteries with long cycling performance, Adv. Funct. Mater. 34 (30) (2024) e2314388, https://doi.org/10.1002/adfm.202314388.

[38] W. Zhang, R. Chen, Y. Dai, X. Wu, J. Chen, W. Zong, M. Zhang, Z. Du, H. Dong, F. Zhao, et al., Asymmetric acceptor–donor small organic molecule enabling versatile and highly-stable aqueous zinc batteries, Mater. Today 78 (2024) 32–45, https://doi.org/10.1016/j.mattod.2024.06.016.

[39] T. Yan, B. Wu, S. Liu, M. Tao, J. Liang, M. Li, C. Xiang, Z. Cui, L. Du, Z. Liang, et al., Sieving-type electric double layer with hydrogen bond interlocking to stable zinc metal anode, Angew. Chem.Int. Edit. 63 (47) (2024) e202411470, https://doi.org/10.1002/anie.202411470.

[40] J. Xu, P. Han, Y. Jin, H. Lu, B. Sun, B. Gao, T. He, X. Xu, N. Pinna, G. Wang, Hybrid molecular sieve-based interfacial layer with physical confinement and desolvation effect for dendrite-free zinc metal anodes, ACS Nano 18 (28) (2024) 18592–18603, https://doi.org/10.1021/acsnano.4c04632.

[41] X. Li, D. Qiu, Q. Zhou, Z. Yang, X. Zhou, W. Wang, C. Wei, T. Zou, Y. Yu, Construction of an anti-anionic-depletion layer to mitigate the tip deposition effect for dendrite-free zinc anode, Chem. Eng. J. 495 (1) (2024) 153855, https://doi.org/10.1016/j.cej.2024.153855.

[42] Z. Bao, Y. Wang, L. Sun, B. Luo, G. Duan, S. Zheng, Z. Ye, J. Huang, Molecular Filter Net Synergy with Regulation in Ion Percolation for High-Performance Zn Metal Batteries, ACS Nano 18 (35) (2024) 24350–24363, https://doi.org/10.1021/acsnano.4c06588.

[43] S. Zhao, X. Liu, T. Chang, H. Tang, T. Tian, Q. Weng, T. Liu, Achieving Stable Zn Anodes by reducing desolvation barrier and guiding homogeneous nucleation through zincophilic polymer layer, Energy Storage Mater. 72 (2024) 103769, https://doi.org/10.1016/j.ensm.2024.103769.

[44] V. Mathew, N.B. Schorr, B. Sambandam, T.N. Lambert, J. Kim, A Critical comparison of mildly acidic versus alkaline zinc batteries, Accounts Mater. Res. 4 (4) (2023) 299–306, https://doi.org/10.1021/accountsmr.2c00221.

[45] D. Yuan, J. Zhao, H. Ren, Y. Chen, R. Chua, E.T.J. Jie, Y. Cai, E. Edison, W. Manalastas Jr., M.W.;. Wong, et al., Anion texturing towards dendrite-free Zn Anode for aqueous rechargeable batteries, Angew. Chem.Int. Edit. 60 (13) (2021) 7213–7219, https://doi.org/10.1002/anie.202015488.

[46] W. Bi, J. Chai, L. Meng, Z. Li, T. Xiong, J. Shu, X. Yao, Z. Peng, Zn-Alloying Sites with Self-Adsorbed Molecular Crowding Layer as a Stable Interfacial Structure of Zn Electrodes, ACS Appl. Mater. Interfaces 15 (21) (2023) 25594–25603, https://doi.org/10.1021/acsami.3c04025.
[47] J. Yang, H. Yan, H. Hao, Y. Song, Y. Li, Q. Liu, A. Tang, Synergetic modulation on solvation structure and electrode interface enables a highly reversible zinc Anode for zinc–iron flow batteries, ACS Energy Lett. 7 (7) (2022) 2331–2339, https://doi.org/10.1021/acsenergylett.2c00560.
[48] P. Ruan, X. Chen, L. Qin, Y. Tang, B. Lu, Z. Zeng, S. Liang, J. Zhou, Achieving highly proton-Resistant Zn-Pb Anode through low hydrogen affinity and strong bonding for long-life electrolytic Zn//MnO(2) Battery, Adv. Mater. 35 (31) (2023) 2300577, https://doi.org/10.1002/adma.202300577.
[49] H. Zhang, S. Li, L. Xu, R. Momen, W. Deng, J. Hu, G. Zou, H. Hou, X. Ji, High-yield carbon dots interlayer for ultra-stable zinc batteries, Adv. Energy Mater. 12 (26) (2022) 2200665, https://doi.org/10.1002/aenm.202200665.
[50] J. He, Y. Tang, G. Liu, H. Li, M. Ye, Y. Zhang, Q. Yang, X. Liu, C. Li, Intrinsic hydrogen-bond donors-lined organophosphate superionic nanochannels levering high-rate-endurable aqueous Zn batteries, Adv. Energy Mater. 12 (46) (2022) 2202661, https://doi.org/10.1002/aenm.202202661.
[51] T. Wang, P. Wang, L. Pan, Z. He, L. Dai, L. Wang, S. Liu, S.C. Jun, B. Lu, S. Liang, et al., Stabling zinc metal anode with polydopamine regulation through dual effects of fast desolvation and ion confinement, Adv. Energy Mater. 13 (5) (2022) 2203523, https://doi.org/10.1002/aenm.202203523.
[52] M. Zhang, W. Xu, X. Han, H. Fan, T. Chen, Y. Yang, Y. Gao, C. Zheng, Y. Yang, T. Xiong, et al., Unveiling The Mechanism of The Dendrite Nucleation and Growth in Aqueous Zinc Ion Batteries, Adv. Energy Mater. 14 (9) (2023) 2303737, https://doi.org/10.1002/aenm.202303737.
[53] Y. Zhou, J. Xia, J. Di, Z. Sun, L. Zhao, L. Li, Y. Wu, L. Dong, X. Wang, Q. Li, Ultrahigh-Rate Zn Stripping and Plating by Capacitive Charge Carriers Enrichment Boosting Zn-Based Energy Storage, Adv. Energy Mater. 13 (10) (2023) 2203165, https://doi.org/10.1002/aenm.202203165.
[54] P. Wu, L. Xu, X. Xiao, X. Ye, Y. Meng, S. Liu, An Industrially Applicable Passivation Strategy for Significantly Improving Cyclability of Zinc Metal Anodes in Aqueous Batteries, Adv. Mater. 36 (2) (2023) 2306601, https://doi.org/10.1002/adma.202306601.
[55] S. Zhao, Y. Zhang, J. Li, L. Qi, Y. Tang, J. Zhu, J. Zhi, F. Huang, A Heteroanionic Zinc Ion Conductor for Dendrite-Free Zn Metal Anodes, Adv. Mater. 35 (18) (2023) 2300195, https://doi.org/10.1002/adma.202300195.
[56] R. Zhang, Y. Feng, Y. Ni, B. Zhong, M. Peng, T. Sun, S. Chen, H. Wang, Z. Tao, K. Zhang, Bifunctional Interphase with Target-Distributed Desolvation Sites and Directionally Depositional Ion Flux for Sustainable Zinc Anode, Angew. Chem.Int. Edit. 62 (25) (2023) e202304503, https://doi.org/10.1002/anie.202304503.
[57] R. Guo, X. Liu, F. Xia, Y. Jiang, H. Zhang, M. Huang, C. Niu, J. Wu, Y. Zhao, X. Wang, et al., Large-Scale Integration of a Zinc Metasilicate Interface Layer Guiding Well-Regulated Zn Deposition, Adv. Mater. 34 (27) (2022) 2202188, https://doi.org/10.1002/adma.202202188.
[58] J.L. Yang, J. Li, J.W. Zhao, K. Liu, P. Yang, H.J. Fan, Stable Zinc Anode Enabled by Zincophilic Polyanionic Hydrogel Layer, Adv. Mater. 34 (27) (2022) 2202382, https://doi.org/10.1002/adma.202202382.
[59] P. Xiao, Y. Wu, K. Liu, X. Feng, J. Liang, Y. Zhao, C. Wang, X. Xu, T. Zhai, H. Li, An Ultrathin Inorganic Molecular Crystal Interfacial Layer for Stable Zn Anode, Angew. Chem.-Int. Edit. 62 (40) (2023) 202309765, https://doi.org/10.1002/anie.202309765.
[60] X. Zhu, W. Zhang, Z. Peng, L. Pan, B. Li, Z. Zhang, J. Zhu, W. Meng, L. Dai, L. Wang, et al., Zinc-tin binary alloy interphase for zinc metal batteries, Chem. Eng. J. 499 (1) (2024) 156521, https://doi.org/10.1016/j.cej.2024.156521.
[61] Y. Xin, J. Qi, H. Xie, Y. Ge, Z. Wang, F. Zhang, B. He, S. Wang, H. Tian, 3D Ternary Alloy Artificial Interphase Toward Ultra-Stable and Dendrite-Free Aqueous Zinc Batteries, Adv. Funct. Mater. 34 (39) (2024) 2403222, https://doi.org/10.1002/adfm.202403222.
[62] Z. Xu, H. Li, Y. Liu, K. Wang, H. Wang, M. Ge, J. Xie, J. Li, Z. Wen, H. Pan, et al., Durable modulation of Zn(002) plane deposition via reproducible zincophilic carbon quantum dots towards low N/P ratio zinc-ion batteries, Mater. Horizons 10 (9) (2023) 3680–3693, https://doi.org/10.1039/d3mh00261f.